

1 **EVALUATION OF CLOUDS, RADIATION, AND PRECIPITATION IN CMIP6**  
2 **MODELS USING GLOBAL WEATHER STATES DERIVED FROM ISCCP-H CLOUD**  
3 **PROPERTY DATA**

4

5 **George Tselioudis<sup>1,2</sup>, William. B. Rossow<sup>3</sup>, Christian Jakob<sup>4</sup>, Jasmine Remillard<sup>1,5</sup>, Derek**  
6 **Tropf<sup>1,5</sup>, and Yuanchong Zhang<sup>1,5</sup>**

7

8

9 1. NASA/GISS, New York, NY

10 2. Columbia University, Dept. of Applied Physics and Applied Math, New York, NY

11 3. Franklin, NY

12 4. ARC Centre of Excellence for Climate Extremes, Monash University, Melbourne,  
13 Australia

14 5. SciSpace, New York, NY

15

16 Corresponding Author:

17 George Tselioudis

18 NASA/GISS

19 2880 Broadway

20 New York, NY 10025

21 USA

22 Email: [George.tselioudis@nasa.gov](mailto:George.tselioudis@nasa.gov)

23

24 **ABSTRACT**

25

26 A clustering methodology is applied to cloud optical depth cloud top pressure (TAU-PC)  
27 histograms from the new, 1-degree resolution, ISCCP-H dataset, to derive an updated global  
28 Weather State (WS) dataset. Then, PC-TAU histograms from current-climate CMIP6 model  
29 simulations are assigned to the ISCCP-H WSs along with their concurrent radiation and  
30 precipitation properties, to evaluate model cloud, radiation, and precipitation properties in the  
31 context of the Weather States. The new ISCCP-H analysis produces WSs that are very similar to  
32 those previously found in the lower resolution ISCCP-D dataset. The main difference lies in the  
33 splitting of the ISCCP-D thin stratocumulus WS between the ISCCP-H shallow cumulus and  
34 stratocumulus WSs, which results in the reduction by one of the total WS number. The  
35 evaluation of the CMIP6 models against the ISCCP-H Weather States, shows that, in the  
36 ensemble mean, the models are producing an adequate representation of the frequency and  
37 geographical distribution of the WSs, with measurable improvements compared to the WSs  
38 derived for the CMIP5 ensemble. However, the frequency of shallow cumulus clouds continues  
39 to be underestimated, and, in some WSs the good agreement of the ensemble mean with  
40 observations comes from averaging models that significantly overpredict and underpredict the  
41 ISCCP-H WS frequency. In addition, significant biases exist in the internal cloud properties of  
42 the model WSs, such as the model underestimation of cloud fraction in middle-top clouds and  
43 secondarily in midlatitude storm and stratocumulus clouds, that result in an underestimation of  
44 cloud SW cooling in those regimes.

45

46

47 **1. Introduction**

48

49 Satellite observations of cloud properties have been used to evaluate climate models ever since  
50 the TIROS meteorological satellites, launched by NASA in the 1960s, provided the first remote  
51 retrievals of global cloud cover (e.g. Somerville et al. 1974). Two main objectives of those cloud  
52 evaluation efforts were to inform model developers of the deficiencies in the model cloud field  
53 so as to assist in improving cloud parameterizations in future model versions, and to increase our  
54 understanding of cloud related processes that play key roles in cloud climate feedbacks.

55 Originally cloud fraction was the only observational field available for evaluation; but since the  
56 advent of the International Satellite Cloud Climatology Project (ISCCP, Rossow and Schiffer  
57 1991), the launch of microwave radiometers like SSMI (Ferraro et al. 1996) and active sensing  
58 instruments like Radars and LiDARs on CloudSat and CALIPSO (Stephens et al. 2008, Winker  
59 et al. 2009), additional cloud properties like top pressure, optical thickness, liquid water path,  
60 and vertical extent were included in the model evaluation comparisons. For a long while, those  
61 evaluations were based on comparisons of time- and space-mean cloud fields, often one at a time  
62 and independent from the coincident properties of the atmosphere (e.g. Hansen et al. 1983,  
63 Schmidt et al. 2006). These comparisons provided quantitative measures of the deficiencies of  
64 the properties of the simulated clouds but did not provide information on the connections  
65 between the properties of the cloud field and the coincident atmospheric state and processes. As  
66 a result, this type of analysis often did not provide modelers with sufficient leads to the  
67 components of the model parameterizations that could be responsible for the cloud property  
68 deficiencies, and did not provide information on the mechanics of cloud related processes that  
69 could be responsible for cloud climate feedbacks.

70

71 This pointed to the need to develop more process-based model evaluation techniques, and several  
72 methods were developed with the aim to sample observational data into distinct regimes and  
73 evaluate model cloud properties within each regime. The regime definition methods that were  
74 applied can be divided into two broad categories. In the first category, one or more atmospheric  
75 parameters were used to derive a dynamic or thermodynamic regime in observations and models,  
76 and the model clouds were evaluated in that particular regime. Following this methodology,  
77 model clouds were evaluated, among others, in tropical and midlatitude ascending and  
78 descending motion regimes (Bony and Dufrense 2005, Tselioudis and Jakob 2002), in combined  
79 vertical motion/boundary layer stability regimes (Grise and Madeiros 2016), and in midlatitude  
80 storm composites (Bodas-Salcedo et al. 2014). These analyses put model cloud deficiencies in  
81 the context of atmospheric processes, showing for example that model boundary layer cloud  
82 cover was deficient in subsidence regimes in general (Bony and Dufrense 2005, Tselioudis and  
83 Jakob 2002) and in midlatitude cold air outbreaks in particular (Bodas Salcedo et al. 2014), and  
84 that this low cloud bias may be in part due to a stronger than observed dependence of model  
85 cloud formation on vertical velocity and a weaker than observed dependence on boundary layer  
86 stability (Grise and Madeiros 2016).

87

88 In the second regime definition category, data mining techniques such as cluster analysis or  
89 neural networks are applied to the cloud properties themselves in order to extract cloud-defined  
90 regimes, and the analysis of the atmospheric conditions is subsequently used to understand the  
91 regime behavior. A data mining technique used widely in cloud property analysis relies on the  
92 application of the K-means clustering algorithm (Anderberg 1973) on combined histograms of

93 cloud optical depth ( $\tau$ ) – cloud top pressure (TAU-PC) from the ISCCP or the Moderate  
94 Resolution Imaging Radiospectrometer (MODIS) datasets. The method was first applied to the  
95 2.5-degree, 3-hourly ISCCP-D1 dataset for the region of the Western Pacific (Jakob and  
96 Tselioudis, 2003). It was then extended to the whole tropics in Rossow et al. (2005), and to the  
97 globe in Tselioudis et al. (2013). The derived cluster centroids represented distinct cloud type  
98 distributions characterized by distinct TAU-PC histograms, and were shown to relate to discrete  
99 atmospheric regimes that were termed Weather States (WSs). Application of the same clustering  
100 method to MODIS TAU-PC histograms (Oreopoulos et al. 2014) produced a set of Cloud  
101 Regimes similar in nature to the ISCCP Weather States. The ISCCP-D1 WSs were used in the  
102 evaluation of cloud simulations in the Climate Model Intercomparison phase 3 (CMIP3)  
103 (Williams and Tselioudis 2007, Williams and Webb 2009) and phase 5 (CMIP5) (Jin et al. 2016)  
104 family of models. The analysis of Williams and Webb (2009) showed large model spread and  
105 deficiencies in cumulus congestus (midlevel) and transition (shallow cumulus) clouds in the  
106 extra-tropics, at magnitudes similar to the previously identified model deficiencies in  
107 stratocumulus clouds in the tropics. This led to the more focused analysis of Bodas-Salcedo et al.  
108 (2014), who identified cold air outbreaks behind frontal zones in the Southern Oceans as a major  
109 regime of model cloud deficiencies. Similar deficiencies in CMIP5 model shallow cumulus  
110 clouds in North Atlantic cold air outbreaks was found in Remillard and Tselioudis (2015). The  
111 analysis of Jin et al. (2016) found tendencies in the CMIP5 models to underestimate the  
112 occurrence of optically thin clouds and clouds with mid-level tops, and to perform better in the  
113 simulation of optically thick storm clouds.

114

115 In the past few years, two new sources of data have become available to the science community.  
116 First, a new, 1-degree horizontal resolution version of the ISCCP cloud property products was  
117 introduced (ISCCP-H, Young et al. 2018). At the same time, the latest versions of climate  
118 models were used in the CMIP6 program to perform a suite of present and future climate  
119 simulations. The present study takes advantage of those new resources, by first applying the  
120 clustering methodology of Tselioudis et al. (2013) to the TAU-PC histograms of the ISCCP-H  
121 dataset, in order to derive an updated cloud-defined Weather State dataset. Then, TAU-PC  
122 histograms from the output of the CMIP6 model simulations are assigned to the derived Weather  
123 States along with their concurrent radiation and precipitation properties, with the objective to  
124 create model WS climatologies and to evaluate cloud, radiation, and precipitation properties in  
125 CMIP6 models in the context of the WSs.

126

127

## 128 **2. Datasets and analysis method**

129

### 130 a. ISCCP-H 1-degree dataset.

131

132 A summary description of the new ISCCP-H products is provided by Young et al (2018), with  
133 complete details in the Climate-Algorithm Theoretical Basis Document (Rossow 2017). Overall,  
134 the ISCCP-H cloud property retrievals are very similar to the ISCCP-D ones, with only a few  
135 notable differences. Higher spatial resolution produces a more “U-shaped” distribution of cloud  
136 amount frequencies, hence as also shown below, the frequency of occurrence of completely clear  
137 conditions increases and the total cloud cover for the cloud WSs increases. The only significant

138 change in ISCCP-H cloud amount is a decrease by about 0.1 (absolute) over Antarctica in  
139 summertime, because of the removal of the test on the 3.7micron channel which is not available  
140 over the whole record. Average cloud top pressures in both polar regions increase by 30-40 mb  
141 in winter and decrease by about the same amount in summer relative to the ISCCP-D values, due  
142 mainly to the change in the ancillary atmospheric temperature profile dataset that is used (cloud  
143 top temperatures are nearly the same on average). There is an increase in the amount of high,  
144 thin clouds (identified in the summer where daylight is available), which appears to be consistent  
145 with CALIPSO observations. The final significant change in cloud properties is a decrease of the  
146 cloud top temperature threshold used to separate ice and liquid clouds to 253K from 260K,  
147 which reduces the relative amount of ice clouds in the ISCCP-H dataset.

148

149 b. WS derivation through K-means clustering.

150

151 The method described in detail in Tselioudis et al. (2013) and previous papers (Jacob and  
152 Tselioudis 2003, Rossow et al. 2005), was also used here to perform the cluster analysis of the  
153 ISCCP-H TAU-PC histograms. The K-means clustering algorithm (e.g., Anderberg 1973) was  
154 applied to the cloud fraction vector formed from the histograms of PC-TAU for each 3-hourly, 1-  
155 degree ISCCP-H grid cell over the period July 1983–June 2015, to derive optimized PC-TAU  
156 clusters. Since TAU is only available during daytime in the ISCCP-H dataset, the derived  
157 clusters are also only available for 3-hourly daylight periods. In the cluster analysis, the “best”  
158 (optimum) cluster number K is determined objectively by a set of diagnostic checks, described in  
159 detail in Tselioudis et al. (2013). Briefly, the clustering algorithm is run in consecutive steps with  
160 K increasing by 1, and in every iteration statistical tests are carried out to check four criteria:

161 whether the clustering procedure converges, whether this convergence is insensitive to the set of  
162 centroids used to initiate the algorithm, whether the dispersion of all the vectors in each cluster is  
163 minimized, and finally whether a distinctly new centroid pattern has appeared when increasing K  
164 by 1 from the previous set of clusters. Note that grid points that are completely cloud free are not  
165 included in the cluster analysis process and form their own clear sky category.

166

167 Based on the above criteria, the method is applied on the ISCCP-H TAU-PC histograms. The  
168 analysis produces a set of 10 cloud Weather States as the most stable result, and the dataset and  
169 plots for the ISCCP-H Weather States are archived and presented at:

170 <http://isccp.giss.nasa.gov/wstates/hggws.html>. The cluster analysis of the ISCCP-H data yields  
171 two pairs of WSs that include very similar TAU-PC histograms and geographical distributions,  
172 with the only difference between them being the mean optical thickness of the two cloud clusters  
173 involved. Specifically, the clustering algorithm produces an optically thinner and an optically  
174 thicker cirrus WS (WS3 and WS6 respectively in the original set) as well as an optically thinner  
175 and an optically thicker stratocumulus WS (WS9 and WS10), with both pairs having very similar  
176 geographical distributions. Since the present paper focuses on the evaluation of the performance  
177 of a large model ensemble in simulating the properties of the observational WSs, to achieve  
178 better clarity for the evaluation results it was decided to merge those two pairs into one cirrus  
179 and one stratocumulus WS (WS3 and WS8 respectively in the merged set). The merging is done  
180 by creating two new WSs that include all grid cells assigned to the optically thin and thick cirrus  
181 and stratocumulus WSs respectively and are represented by the weighted average PC-TAU  
182 histogram of the original WSs. This results in the set of the eight cloud WSs presented and used  
183 in this paper. Any studies that require a more detailed resolution of the cirrus and stratocumulus

184 cloud fields, such as a more detailed model evaluation of those WSs, can be done by accessing  
185 the more detailed, ten cloud WS dataset that is archived in the ISCCP WS web page provided  
186 above.

187

188 c. Model evaluation through WS assignment.

189

190 Climate model AMIP simulations of the 20<sup>th</sup> century are evaluated in this study using the  
191 ISCCP-H Weather States. The models that are used in the analysis are all the ones that provide  
192 output from the application of an ISCCP simulator package (Bodas-Salcedo et al. 2011), which  
193 derives daily TAU-PC histograms from model cloud parameters. A list of the CMIP6 models  
194 that are used, along with their horizontal and vertical resolutions is provided in Table 1. The  
195 majority of the models have horizontal resolutions close to the 1-degree resolution of the ISCCP-  
196 H dataset, with two models having resolutions closer to 2 degrees. Note that when this resolution  
197 effect was tested by degrading the ISCCP-H data to 2 degrees and repeating the WS assignment,  
198 the resulting WS dataset was almost identical with the 1-degree version, implying that the model  
199 resolution differences should not introduce discernable biases to the evaluation. To create a  
200 model WS climatology, each daily model TAU-PC histogram is assigned to the ISCCP-H WS  
201 with which it has the smallest Euclidian distance, and the derived model WS frequencies and  
202 cloud properties are evaluated against the corresponding ISCCP-H ones. In order to perform  
203 comparisons of compatible model-observations quantities, a modified ISCCP-H WS dataset is  
204 created through assignment of daily, rather than 3-hourly, ISCCP-H TAU-PC histograms to the  
205 WS centroids. The result of the transition to the daily ISCCP-H WSs is a significant reduction in  
206 the clear sky occurrence with smaller reductions in all high cloud-fraction WSs, and a

207 corresponding significant increase in the fair weather WS and a smaller increase in the cirrus  
208 WS. Once model WSs are assigned to ISCCP-H WSs, model radiation and precipitation  
209 composites for each WS are constructed and evaluated against analogous ISCCP composites,  
210 which are derived using for radiation the ISCCP-FH dataset (available at:  
211 <https://isccp.giss.nasa.gov/projects/flux.html>), and the CERES dataset (Loeb et al. 2018), and for  
212 precipitation the TRMM-3B42 (Huffman et al. 2007) dataset. Note that in order to map changes  
213 in the model cloud WS frequency and properties between the CMIP5 and CMIP6 model  
214 ensembles, the WS analysis is also performed on CMIP5 output of the previous generation of the  
215 analyzed CMIP6 models.

216

217

### 218 **3. Results**

219

#### 220 a. Merged ISCCP-H Weather States

221

222 Figure 1 shows the TAU-PC histograms of the 8 cloud WSs derived from the cluster analysis of  
223 the 1-degree resolution ISCCP-H data and the subsequent merging (top), along with global maps  
224 of the Relative Frequency of Occurrence (RFO) of each WS and of clear sky (bottom). The WS  
225 histograms are arranged as follows. The top three categories include high-top cloud WSs, namely  
226 optically thick tropical deep convective and anvil clouds (WS1-DCN), somewhat lower-top and  
227 optically thick midlatitude storm clouds (WS2-MDS), and optically thin high cirrus clouds  
228 (WS3-CIR). Those three high cloud categories occur 6.7%, 9.5%, and 15.9% of the time  
229 respectively, and while the deep convective and storm cloud WSs are practically overcast, the

230 cirrus WS has a cloud cover of about 80%. The latter may be in part due to the fact that the  
231 ISCCP satellite retrievals miss the thinnest cirrus clouds (Stubenrauch *et al.* 2013). The next two  
232 categories include polar clouds that show a mix of various top heights and optical thicknesses  
233 with an RFO of 3% and a cloud cover of 84.5% (WS4-PLR), and optically thick and nearly  
234 overcast middle-top clouds (WS5-MID) that occur 6.1% of the time. Then there is the fair-  
235 weather (WS6-FRW) category that has the lowest cloud cover (40%) and the highest frequency  
236 of occurrence (37.5%), and includes mostly scattered thin cumulus and cirrus clouds. Finally,  
237 there are the two low-top cloud categories. The first includes optically thinner and lower cloud-  
238 top shallow cumulus clouds (WS7-SHC), which have a large cloud cover (79.6%) that indicates  
239 systemic organization rather than a scattered cloud field. The second includes optically thicker  
240 low clouds with larger cloud cover (90.7%) and higher cloud top, indicative of stratocumulus  
241 clouds (WS8-STC). The ninth Weather State (WS9-CLR) represents completely cloud-free grid  
242 boxes, which occur 4.2% of the time and were not included in the clustering analysis. Table 2  
243 lists the average cloud top pressure, cloud optical thickness, and cloud cover of all eight cloud  
244 WSs.

245

246 The WS RFO maps (Fig.1-bottom) show that deep convective clouds (WS1) are concentrated  
247 primarily in the ITCZ/SPCZ region, with a small concentration in the entry regions of the  
248 northern midlatitude storm tracks near the west coasts of the Northern continents. Cirrus clouds  
249 (WS3) occur both in the ITCZ, with larger concentrations in the tropical West Pacific and Indian  
250 oceans, and in the vicinity of large mountain ranges like the Himalayas, Rockies, and Andes. The  
251 midlatitude storm clouds (WS2) occur in the core of the midlatitude storm tracks, while the  
252 middle top (WS5) and the organized shallow cumulus (WS7) clouds occur primarily in the

253 poleward and equatorward edges of the storm tracks respectively. The polar clouds (WS4) are  
254 well confined in the polar regions, and the stratocumulus clouds (WS8) occur mostly off the  
255 western coasts of the main continents, with additional occurrence in the midlatitude storm tracks.  
256 The fair-weather cloud WS shows high populations in the middle of the tropical and subtropical  
257 ocean basins and in the polar regions.

258

259 The ISCCP-H WSs are very similar to the lower resolution ISCCP-D WSs (Tselioudis et al.  
260 2013), with only one significant difference: while the ISCCP-D analysis produced three  
261 stratocumulus WSs of low, medium, and high optical thickness, the ISCCP-H cluster analysis  
262 splits the low optical thickness stratocumulus WS between the shallow cumulus and the medium  
263 thickness stratocumulus WSs, thus producing two stratocumulus WSs of medium and high  
264 optical thickness and reducing the total number of WS by one. Note, however, that in the merged  
265 analysis presented in this paper the two ISCCP-H stratocumulus WSs were further combined into  
266 one WS8-STC. Furthermore, the ISCCP-H cluster analysis produces a polar WS that is much  
267 better confined to the polar regions than the corresponding one in the ISCCP-D analysis. Finally,  
268 due to its higher resolution, the ISCCP-H WS set has a 2% higher amount of cloud free boxes  
269 than the ISCCP-D WS set and a little higher total cloud cover in all WS categories.

270

271 The vertical structure of the merged ISCCP-H WSs is shown in Figure 2, derived from analysis  
272 of coincident retrievals from the CloudSat/CALIPSO Radar/LiDAR active measurements. The  
273 independently derived vertical profiles from the active instruments fall well within the cloud type  
274 assumptions derived from the radiatively derived ISCCP-H TAU-PC histograms. They show that  
275 deep convection and midlatitude storm cloud WSs consist primarily of extensive cloud layers

276 that cover the depth of the troposphere, cirrus clouds consist of thin high cloud layers,  
277 stratocumulus and shallow cumulus clouds consist of mostly isolated low cloud layers, while  
278 middle-top clouds consist of layers that top in the middle troposphere but also of coincident low  
279 and cirrus clouds, a situation that produces a mid-troposphere radiative IR signature (cf. Jin and  
280 Rossow 1997). The radar/lidar confirm the presence of more high-top and fewer low-top clouds  
281 in the ISCCP-H polar WS than its ISCCP-D counterpart, due to both the better restriction of this  
282 WS to the polar regions and to an increase in ISCCP-H high cloud detections in that region.  
283 Some of the cirrus missed by ISCCP appears in the composite radar/lidar for WS9 (CLR). In  
284 general, the vertical cloud structures in Fig. 2 appear to be less of a mixture of cloud layers and  
285 to have more distinct layer structures than the equivalent ones for ISCCP-D (Tselioudis *et al.*  
286 2013).

287

288 The WSs derived from the cluster analysis of the TAU-PC histograms are named after cloud  
289 types that are customarily associated with morphological cloud characteristics, often visible in  
290 satellite images. An attempt to associate the WSs to cloud morphological features observed in  
291 satellite images is shown in Figure 3, where a grid of the derived WSs with their assigned  
292 number is overlaid on a visible image from the MODIS instrument on the Aqua satellite, for the  
293 case of a midlatitude storm system that covers most of the North Atlantic region. It can be seen  
294 that the cold and warm frontal conveyor belts of the storm are dominated by midlatitude storm  
295 WS2-MDS clouds, along with some embedded deep convective WS1-DCN clouds occurring  
296 mostly in the northern storm edge where the warm conveyor belt wraps around the low-pressure  
297 center. The WSs occurring in the cold air outbreak region behind the front can be seen as a  
298 transition between two distinct regimes. The regime in the northwestern region of the storm,

299 where the continental cold/dry air flows over the warm Gulf Stream waters, and which is  
300 dominated by nearly overcast middle-top WS5-MID and stratocumulus WS8-STC clouds, and  
301 the regime further downstream, where, as the thicker cloud deck breaks up and cloud cover  
302 decreases, the region is dominated by shallow cumulus WS7-SHC. The pre-frontal maritime and  
303 post-frontal continental regions are dominated by fair weather WS6-FRW clouds. Note that the  
304 figure is a compilation of two Aqua overpasses that took place within the 3-hour window of the  
305 ISCCP observation, so there is some uncertainty in the observation time and exact time  
306 correspondence of each grid box with ISCCP cannot be expected. However, the figure  
307 demonstrates that the cloud types defined through the cluster analysis of the ISCCP TAU-PC  
308 histograms correspond closely with the dynamic regimes where those cloud types are expected to  
309 occur (cf. Lau and Crane 1995, Tselioudis et al 2013).

310

#### 311 b. Weather State Dynamical Characteristics

312

313 The WS variability in the context of the conveyor belts of a midlatitude storm depicted in Fig. 3  
314 shows the strong dynamical controls on cloud property distribution. Model cloud deficiencies  
315 often occur in specific dynamic regimes, and clouds occurring in post-frontal cold air outbreaks  
316 have been identified as primary sources of model error in previous evaluations of CMIP3 and  
317 CMIP5 models (e.g. Williams and Webb 2008, Bodas-Salcedo et al. 2014). These low and  
318 middle top cloud structures have distinct radiative characteristics and occur when particular  
319 combinations of dynamic and thermodynamic conditions are present. In addition, getting the  
320 atmospheric heating and cooling by the characteristic WS right is crucial to the feedbacks on the  
321 atmospheric dynamics (cf. Rossow *et al.* 2016). In order to start resolving the distinct dynamic

322 conditions under which the different WSs are formed, Figure 4 shows the distribution of mid-  
323 tropospheric vertical velocity for each WS by plotting the WS box-and-whisker diagrams of  
324 ERA-Interim 500-mb vertical velocity (Dee et al. 2011). The vertical velocity distributions show  
325 a regular progression, going from strong ascending motion in convective and storm clouds, to a  
326 mixed motion regime in cirrus and middle top clouds, to a descending regime in low top clouds,  
327 similar to the progression found for the ISCCP-D WSs in Tselioudis et al. (2013). However, Fig.  
328 4 shows that groupings of WSs have similar vertical velocity distributions, with small differences  
329 only in the distribution width or the length of the tails. Stratocumulus and shallow cumulus  
330 clouds, for example, both occur primarily in moderate descending motion and have distribution  
331 tails reaching into the strong descending and weak ascending motion, with shallow cumulus  
332 clouds showing greater width and tail variability.

333

334 Since vertical motion by itself only resolves broad differences between ascending and  
335 descending cloud regimes, a second layer of dynamical complexity can be added by looking at  
336 the differences in WS horizontal winds. Figure 5 shows wind roses of the 850mb wind from  
337 ERA-Interim (Dee et al. 2011) for each WS, illustrating wind direction and speed together with  
338 the relative occurrence of each wind subdivision. Note that Southern Hemisphere meridional  
339 wind direction has been reversed so that in the plot Northerly wind always implies an  
340 equatorward direction. At the top of each plot, the label shows the percentage of time that each  
341 WS occurs in the tropical, midlatitude, and polar regions. Most WS wind roses include one  
342 dominant wind direction regime, but several WSs show a second significant regime as well.  
343 Overall, the more tropical WSs (DCN, CIR, FRW) occur under the influence of easterly trade  
344 winds, but deep convection has a significant southwesterly wind component coming potentially

345 from convection embedded in midlatitude storm systems and from convection formed during the  
346 summer Asian monsoon. The more midlatitude WSs (MDS, MID) and the polar WS are  
347 dominated by westerly winds characteristic of the baroclinic jet regime, with the midlatitude  
348 storm WS showing a southwesterly component typical of the cold-frontal conveyor belt and the  
349 middle top WS showing a northwesterly component typical of the post-frontal cold air outbreak  
350 circulation. The stratocumulus and shallow cumulus WSs show almost equal frequency of  
351 occurrence in tropical and midlatitude regions, and both include a prominent northeasterly wind  
352 component characteristic of the trade wind regime and a secondary but still significant  
353 northwesterly component characteristic of the post-frontal circulation.

354

355 This further separation of WSs in horizontal wind regimes indicates that stratocumulus and  
356 shallow cumulus cloud structures, with similar radiative characteristics and even dynamical  
357 environments as far as the vertical motion field is concerned, can occur in two distinct dynamic  
358 regimes as defined by the horizontal wind: in cold air outbreaks behind frontal systems and in  
359 easterly trade wind regimes. This implies that clouds in those WSs can be formed through two  
360 distinct stratocumulus-to-shallow cumulus transition mechanisms; one in which cloud formation  
361 is driven by surface latent heating and boundary layer instability and cloud breakup by  
362 precipitation onset (Fig. 3), and the other in which cloud formation is driven by cloud-top  
363 radiative heating and turbulence and cloud break-up by dry air entrainment. In order to  
364 distinguish between the two different stratocumulus and shallow cumulus dynamic regimes, the  
365 STC and SHC WSs are split into their westward and eastward horizontal wind components using  
366 the 850mb wind plotted in Figure 6. The resulting TAU-PC histograms (not shown) are very  
367 similar, with slightly higher optical thickness for the westward components, and the global RFO

368 numbers are split almost evenly between the easterly-westerly components (4.9%-4.4% for STC,  
369 3.6%-4% for SHC). The resulting RFO global maps are shown in Figure 6, for the STC WS at  
370 the top and the SHC WS at the bottom. It can be seen that the splitting by the horizontal wind  
371 regime clearly separates the midlatitude from the tropical components of the stratocumulus and  
372 shallow cumulus WSs, thus making possible more targeted studies of the mechanisms involved  
373 in the two different cloud transitions.

374

375

### 376 c. CMIP6 Model Cloud Evaluation

377

378 The Relative Frequency of Occurrence (RFO) of the merged H-WSs from the ensemble of  
379 CMIP6 model AMIP simulations that provided the necessary TAU-PC histograms at daily  
380 resolution is shown in Figure 7, together with the daily merged ISCCP-H WS RFO. Note that the  
381 model WSs are derived through assignment of each model TAU-PC histogram to the ISCCP WS  
382 with which it has the smallest Euclidian distance. The figure also shows the model ensemble  
383 mean, and with smaller symbols the WS distributions of an ensemble of CMIP5 models which  
384 contains the earlier versions of the same models included in the CMIP6 ensemble. For most WSs  
385 the ensemble mean RFO of the CMIP6 models falls within or just outside the limits of the  
386 observational uncertainty, with the notable exception of the clear sky fractions that are  
387 significantly higher in all models than in the satellite retrievals. The main reason for this  
388 difference is that over the Sahara and Arabian deserts the models tend to simulate frequent  
389 daylight clear sky conditions while the satellites retrieve mostly fair-weather clouds. The good  
390 agreement of the model ensemble mean with observations shown in Fig. 4 is in several WSs the

391 result of a wide spread of model RFO values located on either side of the observed value.  
392 Moreover, systematic biases, with all or most models biased in the same direction, exist in  
393 several WSs. The most pronounced systematic bias occurs in the shallow cumulus WS, where all  
394 but two models significantly underestimate the RFO amount. Smaller systematic RFO biases  
395 exist in fair weather and deep convective clouds, where most CMIP6 models fall below the  
396 ISCCP line. The underestimate of shallow cumulus clouds found in both CMIP6 and CMIP5  
397 ensembles has also been noted in several previous analyses of CMIP5 simulations (e.g. Bodas-  
398 Salcedo et al. 2014, Remillard and Tselioudis 2015) and was attributed to cloud underestimation  
399 in cold air outbreaks behind midlatitude frontal systems, while the underestimate of midlevel  
400 cloud was also found in the WS analysis of CMIP5 models of Jin et al. (2016).

401  
402 As noted before, in addition to the systematic model biases, in several WSs the models tend to  
403 fall into two contrasting groups that severely underestimate and severely overestimate  
404 respectively the ISCCP-H WS RFO values. In order to quantify the CMIP6 model RFO bias  
405 spread in a way that avoids the positive and negative bias cancellations of the averaging Table 3  
406 shows the WS RFO absolute deviation in % of the CMIP6 and CMIP5 model ensembles from  
407 the observed RFO, normalized by the observed RFO value. It can be seen that in the CMIP6  
408 model ensemble the absolute WS RFO deviation is above 30% of the observational value for the  
409 cirrus, polar, stratocumulus, mid-level, and shallow cumulus WSs, implying that the model  
410 ensemble mean agreement with the observations often results from the averaging of significant  
411 contrasting biases. Compared to the CMIP5 ensemble, the CMIP6 models show in five cloud  
412 WSs RFO absolute deviation values that are smaller than the CMIP5 model ones, thus resulting

413 in a smaller overall mean deviation and implying an improved representation of the WS RFO  
414 distribution by the CMIP6 models.

415

416 As noted before, the WS assignment for the models is done through closest association of the  
417 model PC-TAU histograms with the ISCCP WSs, implying that the resulting model WSs can  
418 still differ significantly in their cloud cover, optical thickness, or cloud top pressure values or  
419 their geographical distribution from the ISCCP WS to which they are assigned. Those  
420 differences, which can result in model radiation or precipitation biases even in cases of correct  
421 WS RFO representations, are examined in Figure 8. The figure shows for each WS the model  
422 difference in (from top) mean cloud fraction, mean optical depth, and mean cloud top pressure  
423 from the corresponding ISCCP WS, and (bottom) the RMS difference of WS geographical  
424 pattern derived through differencing of the WS RFO maps of each model from the corresponding  
425 ISCCP maps. The CMIP5 model ensemble mean is also plotted on all the panels. It can be seen  
426 that with the only major exception of the shallow cumulus WS, CMIP6 models tend to  
427 underestimate WS cloud fraction by about 4-6%, and the underestimation is smaller than in  
428 CMIP5 models for most WSs. This difference, however, can be in part due to the generally lower  
429 horizontal model resolutions in the CMIP5 ensemble. At the same time, model cloud optical  
430 depth is higher than ISCCP in five WSs, the same in two, and lower only in polar clouds, but the  
431 polar model overestimation could be due to underestimation of cloud optical depth in ISCCP  
432 retrievals over ice surfaces. The CMIP5 ensemble similarly has higher optical depth than ISCCP  
433 in most WSs. Overall, it can be said that CMIP6 models still follow the “too few-too bright”  
434 paradigm found in all previous generations of climate models (e.g. Webb et al. 2001, Weare  
435 2004, Karlsson et al. 2008, Nam et al. 2012). The cloud top pressure of the deep convective and

436 midlatitude storm WSs is larger than that found in ISCCP implying generally lower cloud tops in  
437 the model simulations, while for most other WSs the cloud top pressures are generally lower than  
438 in ISCCP indicating higher model cloud tops for cirrus, polar, and all low clouds. The bias for  
439 low cloud top pressures may be even worse because the ISCCP-H estimates seem to be biased  
440 low (Stubenrauch *et al.* 2013). Finally, the RFO geographical pattern differences between the  
441 CMIP6 model and ISCCP WSs are very small for deep convective, midlatitude storm, middle-  
442 top, and shallow cumulus WSs, meaning that the cloud types that are associated with the ITCZ  
443 and the midlatitude storm tracks show almost identical patterns with the observed ones. The  
444 cirrus and fair weather WSs, cloud types that tend to be more widespread, show the largest  
445 pattern differences from the observations. Note, however, that part of the difference in the  
446 pattern may represent difference in the RFO values between the model and ISCCP WSs. The WS  
447 pattern biases found in the present analysis are similar between the CMIP6 and CMIP5  
448 ensembles and are both significantly smaller than the pattern differences found in a similar  
449 analysis of CMIP3 models by Williams and Webb (2008).

450

451 The distribution of Shortwave and Longwave Cloud Radiative Effect (SWCRE/LWCRE) among  
452 the model Weather States is evaluated in Figure 9 against the observational distributions, derived  
453 from compositing the ISCCP-FH and CERES radiative flux data in the merged ISCCP-H  
454 weather states. The ISCCP-FH radiative flux retrievals are derived through the application of a  
455 radiative flux calculation on the ISCCP-H cloud field, and therefore they represent the radiative  
456 fluxes that the models would calculate if they faithfully simulated the ISCCP-H WS cloud  
457 property distributions. The difference between the ISCCP-FH and the CERES CRE values can  
458 be seen as the observational uncertainty, or even as the ISCCP-FH bias against the more direct

459 CERES flux retrievals. Figure 9 shows that in all WS categories the observational uncertainty is  
460 much smaller than the model spread, and that in certain categories clear model biases can be  
461 identified. The largest model bias occurs in the middle top WS, where the model mean cloud SW  
462 cooling is too small by 20-30W/m<sup>2</sup>, due primarily to the underprediction of cloud fraction in that  
463 WS (cf. Fig. 8). A smaller SWCRE bias occurs in the midlatitude storm and the stratocumulus  
464 WSs, due to the underprediction of cloud fraction despite the overprediction of cloud optical  
465 depth in those categories. In contrast, SWCRE is too strong in shallow cumulus clouds, due to an  
466 overprediction of cloud cover and optical depth in those clouds. In the LWCRE evaluation, the  
467 only clear bias is in the midlatitude storm WS, where the lower model cloud tops and cloud  
468 fraction (Fig.8) result in weaker LW cloud effects in all models. The somewhat weaker LW  
469 warming in the cirrus and middle-top WSs can only be explained by the lower cloud fraction in  
470 those regimes.

471  
472 The distribution of precipitation among the model WS is evaluated in Figure 10, against the same  
473 distribution from a composite of TRMM rain rate retrievals on the merged ISCCP-H weather  
474 states. The large majority of the observed precipitation falls in the deep convective and  
475 midlatitude storm WSs, with contributions from the cirrus (which may be due to platform space-  
476 time mismatch near convective systems) and the middle top WSs, and this distribution is present  
477 in the model simulations as well. However, CMIP6 models show a spread in precipitation rate in  
478 the deep convective and to a lesser extent the storm cloud WS that is very large, with the extreme  
479 models differing by as much as 10-15 mm/day in deep convective precipitation rates. In the  
480 ensemble mean, CMIP6 models simulate higher, more realistic convective precipitation rates  
481 than CMIP5 models. Also, all models tend to show a small overestimation of the low rain rates

482 in all WSs other than the convective and storm cloud ones, indicating the presence of excess  
483 drizzle in the model simulations.

484

485

#### 486 **4. Discussion**

487

488 A cluster analysis of TAU-PC histograms of the new, higher resolution ISCCP-H dataset  
489 produces cloud regimes that are very similar to the lower resolution ISCCP-D WSs. The main  
490 difference lies in the elimination of the ISCCP-D ‘thin stratocumulus’ category and the splitting  
491 of those clouds between the stratocumulus and shallow cumulus ISCCP-H WSs. This happens  
492 because the ISCCP-H dataset resolves better the stratocumulus-to-shallow cumulus transition,  
493 while in the coarser ISCCP-D retrievals the mixed-cloud transition scenes are classified as a thin  
494 stratocumulus category. Another important difference is found in the polar cloud WS, which has  
495 a different, more consistent with the active retrievals TAU-PC distribution than the ISCCP-D one  
496 and is much better confined to the polar regions. The overall consistency between the two ISCCP  
497 WS analyses is indicative of the similarities between the two ISCCP datasets, with the  
498 differences coming mostly from the higher horizontal resolution of the ISCCP-H data and from  
499 the changes in the cloud property retrievals over ice covered surfaces. This implies that results  
500 derived from analyses of the ISCCP-D WSs of Tselioudis et al. (2013) will remain consistent if  
501 the ISCCP-H WSs are used instead, unless polar clouds are the analysis focus.

502

503 The evaluation of the CMIP6 models against Weather States derived from cloud property cluster  
504 analysis, shows that in the ensemble average the models are producing an adequate

505 representation of the frequency and geographical distribution of the WSs, with some  
506 improvements compared to the WSs derived for the CMIP5 ensemble. However, in some WSs  
507 like cirrus and stratocumulus, the good agreement of the model ensemble mean with the  
508 observations comes from averaging two groups of models that significantly overpredict and  
509 underpredict the RFO values. In addition, significant biases exist in the cloud properties of the  
510 model WSs, such as the model underestimation of cloud fraction in middle-top clouds and  
511 secondarily in midlatitude storm and stratocumulus clouds, that result in an underestimation of  
512 cloud SW cooling in those regimes. The cloud defined WSs constitute a useful framework to  
513 initiate a ‘regime based’ evaluation of climate models.

514

515 As shown in the case of the boundary layer clouds, however, cloud distributions with similar  
516 radiative characteristics can still derive from distinct atmospheric processes. In the context of  
517 model evaluation and its use to improve cloud simulations, where knowledge of the mechanisms  
518 involved in cloud formation and dissipation is crucial, it may be necessary to further split the  
519 WSs to obtain consistent dynamic regimes. As an example, Figure 11 shows the evaluation of  
520 the CMIP6 models separately for the RFO of the easterly and westerly components of the SHC  
521 and STC WSs. It can be seen that for the SHC WS, which is underestimated in the whole by the  
522 models (Fig. 7), this underestimate is more pronounced in the tropical (easterly) than in the  
523 midlatitude (westerly) component of the WS. For the STC WS, which is slightly overestimated  
524 in the whole (Fig. 7), this overestimate comes from an underestimate of the tropical component  
525 and an overestimate of the midlatitude one. Overall, models tend to underpredict stratocumulus  
526 and shallow cumulus amounts in the tropical trade wind regime more than in the midlatitude cold  
527 air outbreak regime. This information provides additional insight into the processes that may be

528 responsible for potential model cloud deficiencies, but further dynamical or thermodynamical  
529 compositing may be needed to meaningfully resolve cloud formation and dissipation processes.

530

531 As illustrated in Figure 3 for the case of a midlatitude storm, the cluster analysis derived WSs

532 provide regime definitions that correspond to distinct combinations of dynamic and

533 thermodynamic conditions that result in the formation of the distinct cloud type distributions.

534 The evaluation of CMIP6 climate models using the WS distributions constitutes a meaningful

535 ‘regime-based’ evaluation, which can provide information pointing to the processes responsible

536 for potential model deficiencies. Furthermore, if climate change is seen as a shift in the

537 distribution of atmospheric regimes, then the ability of the models to reproduce the distribution

538 of cloud, radiation, and precipitation properties among the regimes provides a test for their

539 ability to simulate climate feedbacks resulting from atmospheric regime distribution shifts.

540

541

## 542 **DATA AVAILABILITY STATEMENT**

543

544 The ISCCP-H Weather State dataset discussed in this study is available in the following location:

545 <http://isccp.giss.nasa.gov/wstates/hggws.html>

546

547

## 548 **REFERENCES**

549

550 Anderberg, M.R., 1973: Cluster analysis for applications. Elsevier, New York

551

552 Bodas-Salcedo, A., K. D. Williams, M. A. Ringer, I. Beau, J. N. S. Cole, J.-L. Dufresne, T.

553 Koshiro, B. Stevens, Z. Wang, and T. Yokohata, 2014: Origins of the Solar Radiation Biases

554 over the Southern Ocean in CFMIP2 Models. *J. Climate*, **27**, 41–

555 56, <https://doi.org/10.1175/JCLI-D-13-00169.1>.

556

557 Bodas-Salcedo A, Webb MJ, Bony S, H. Chepfer, J. -L. Dufresne, S. A.Klein, Y. Zhang, R.

558 Marchand, J. M. Haynes, R. Pincus, 2011: COSP: satellite simulation software for model

559 assessment. *Bull Am Meteorol Soc* 92:1023–1043. doi:10.1175/2011BAMS2856.1

560

561 Bony, S., and Dufresne, J.-L., 2005: Marine boundary layer clouds at the heart of tropical cloud

562 feedback uncertainties in climate models, *Geophys. Res. Lett.*, 32, L20806,

563 doi:10.1029/2005GL023851.

564

565 Dee, D.P., Uppala, S.M., Simmons, A.J., Berrisford, P., Poli, P., Kobayashi, S., Andrae, U.,

566 Balmaseda, M.A., Balsamo, G., Bauer, P., Bechtold, P., Beljaars, A.C.M., van de Berg, L.,

567 Bidlot, J., Bormann, N., Delsol, C., Dragani, R., Fuentes, M., Geer, A.J., Haimberger, L., Healy,

568 S.B., Hersbach, H., Hólm, E.V., Isaksen, L., Kållberg, P., Köhler, M., Matricardi, M., McNally,

569 A.P., Monge-Sanz, B.M., Morcrette, J.-J., Park, B.-K., Peubey, C., de Rosnay, P., Tavolato, C.,

570 Thépaut, J.-N. and Vitart, F., 2011: The ERA-Interim reanalysis: configuration and performance

571 of the data assimilation system. *Q.J.R. Meteorol. Soc.*, 137: 553-597.

572 <https://doi.org/10.1002/qj.828>

573

574

575 Ferraro, R., N. Grody, F. Weng, and A. Basist, 1996: An eight-year (1987–1994) time series of  
576 rainfall, clouds, water vapor, snow cover, and sea ice derived from SSM/I measurements.

577 *Bulletin of the American Meteorological Society*, **77**, 891–905

578

579 Grise, K. M., and B. Medeiros, 2016: Understanding the varied influence of midlatitude jet  
580 position on clouds and cloud radiative effects in observations and global climate models. *J.*

581 *Climate*, **29**, 9005–9025, <https://doi.org/10.1175/JCLI-D-16-0295.1>.

582

583 Hansen, J., G. Russell, D. Rind, P. Stone, A. Lacis, S. Lebedeff, R. Ruedy, and L. Travis,

584 1983: Efficient three-dimensional global models for climate studies: Models I and II. *Mon.*

585 *Weather Rev.*, **111**, 609–662, doi:10.1175/1520-0493(1983)111<0609:ETDGMF>2.0.CO;2.

586 Huffman, G.J., R.F. Adler, D.T. Bolvin, G. Gu, E.J. Nelkin, K.P. Bowman, Y. Hong, E.F.

587 Stocker, D.B. Wolff, 2007: The TRMM Multi-satellite Precipitation Analysis: Quasi-Global,

588 Multi-Year, Combined-Sensor Precipitation Estimates at Fine Scale. *J. Hydrometeor.*, **8**(1), 38-

589 55.

590

591 Jakob C, Tselioudis G, 2003: Objective identification of cloud regimes in the Tropical Western

592 Pacific. *Geophys Res Lett* **30**:2082. doi:10.1029/2003GL018367

593

594 Jin, D., Oreopoulos, L. & Lee, D., 2017: Regime-based evaluation of cloudiness in CMIP5

595 models. *Clim Dyn* **48**, 89–112. <https://doi.org/10.1007/s00382-016-3064-0>

596

597 Jin, Y, and Rossow, W. B., 1997: Detection of cirrus overlapping low level clouds. *Journal of*  
598 *Geophysical Research* **102**: doi: 10.1029/96JD02996. Issn: 0148-0277.  
599

600 Karlsson, J., G. Svensson, and H. Rodhe, 2008: Cloud radiative forcing of subtropical low level  
601 clouds in global models, *Clim. Dyn.*, 30, 779– 788.  
602

603 Lau, N., & Crane, M. W. (1995). A Satellite View of the Synoptic-Scale Organization of Cloud  
604 Properties in Midlatitude and Tropical Circulation Systems, *Monthly Weather Review*, 123(7),  
605 1984-2006.  
606

607 Loeb, N. G., and Coauthors, 2018: Clouds and the Earth’s Radiant Energy System (CERES)  
608 Energy Balanced and Filled (EBAF) top-of-atmosphere (TOA) Edition-4.0 data product. *J.*  
609 *Climate*, **31**, 895–918, <https://doi.org/10.1175/JCLI-D-17-0208.1>.  
610

611 Nam, C., Bony, S., Dufresne, J.-L., and Chepfer, H., 2012: The ‘too few, too bright’ tropical  
612 low-cloud problem in CMIP5 models, *Geophys. Res. Lett.*, 39, L21801,  
613 doi:10.1029/2012GL053421.  
614

615 Oreopoulos, L., N. Cho, D. Lee, S. Kato, and G. J. Huffman, 2014: An examination of the nature  
616 of global MODIS cloud regimes. *Journal of Geophysical Research: Atmospheres* **119** (13):  
617 8362-8383 [10.1002/2013JD021409]  
618

619 Rémillard, J., and G. Tselioudis, 2015: Cloud regime variability over the Azores and its  
620 application to climate model evaluation. *J. Climate*, **28**, no. 24, 9707-9720, doi:10.1175/JCLI-D-  
621 15-0066.1.

622 Rossow WB, Schiffer RA, 1991: ISCCP cloud data products. *Bull Am Meteorol Soc* 72:2–20.  
623 doi:10.1175/1520-0477(1991)072<0002:ICDP>2.0.CO;2

624 Rossow WB, Tselioudis G, Polak A, Jakob C, 2005: Tropical climate described as a distribution  
625 of weather states indicated by distinct mesoscale cloud property mixtures. *Geophys Res Lett*  
626 32:L21812. doi:10.1029/2005GL024584

627 Rossow, W.B., Y-C. Zhang and G. Tselioudis, 2016: Atmospheric diabatic heating in different  
628 weather states and the general circulation. *J. Climate*, **29**, 1059-1065, doi:10.1175/JCLI-D-15-  
629 0760.1.

630

631 Rossow, W.B., 2017: ISCCP H-Version – Climate Algorithm Theoretical Basis Document,  
632 NOAA Climate Data Record Program (CDRP-ATDB-0.872) Rev 0 (2017), 301 pp. Available at:  
633 [http://www1.ncdc.noaa.gov/pub/data/sds/cdr/CDRs/Cloud\\_Properties-](http://www1.ncdc.noaa.gov/pub/data/sds/cdr/CDRs/Cloud_Properties-)  
634 [ISCCP/AlgorithmDescription\\_01B-29.pdf](http://www1.ncdc.noaa.gov/pub/data/sds/cdr/CDRs/Cloud_Properties-ISCCP/AlgorithmDescription_01B-29.pdf).

635

636 Stubenrauch, C.J., W.B. Rossow, S. Kinne, S.A. Ackerman, G. Cesana, H. Chepfer, B.  
637 Getzewich, L. Di Girolamo, A. Guignard, A. Heidinger, B. Maddux, P. Menzel, P. Minnis,  
638 C. Pearl, S. Platnick, C. Poulsen, J. Reidi, S. Sun-Mack, A. Walther, D. Winker, S. Zeng  
639 and G. Zhao, 2013: Assessment of global cloud datasets from satellites: Project and

640 database initiated by the GEWEX Radiation Panel. *Bull. Amer. Meteor. Soc.*, **94**, 1031-  
641 1049, doi:10.1175/BAMS-D-12-00117.1.

642

643 Schmidt, G.A., R. Ruedy, J.E. Hansen, I. Aleinov, N. Bell, M. Bauer, S. Bauer, B. Cairns, V.  
644 Canuto, Y. Cheng, A. Del Genio, G. Faluvegi, A.D. Friend, T.M. Hall, Y. Hu, M. Kelley, N.Y.  
645 Kiang, D. Koch, A.A. Lacis, J. Lerner, K.K. Lo, R.L. Miller, L. Nazarenko, V. Oinas, J.P.  
646 Perlwitz, J. Perlwitz, D. Rind, A. Romanou, G.L. Russell, M. Sato, D.T. Shindell, P.H. Stone, S.  
647 Sun, N. Tausnev, D. Thresher, and M.-S. Yao, 2006: Present day atmospheric simulations using  
648 GISS ModelE: Comparison to in-situ, satellite and reanalysis data. *J. Climate*, **19**, 153-192,  
649 doi:10.1175/JCLI3612.

650

651 Somerville, R.C.J., P.H. Stone, M. Halem, J.E. Hansen, J.S. Hogan, L.M. Druyan, G.  
652 Russell, A.A. Lacis, W.J. Quirk, and J. Tenenbaum, 1974: The GISS model of the global  
653 atmosphere. *J. Atmos. Sci.*, **31**, 84-117, doi:10.1175/1520-  
654 0469(1974)031<0084:TGMOTG>2.0.CO;2

655 Stephens GL, Vane DG, Tanelli S, 2008: CloudSat mission: performance and early science after  
656 the first year of operation. *J Geophys Res* 113:2156–2202. doi:10.1029/2008JD009982

657

658 Tselioudis, G., and C. Jakob, 2002: Evaluation of midlatitude cloud properties in a weather and a  
659 climate model: Dependence on dynamic regime and spatial resolution. *J. Geophys. Res.*, **107**, no.  
660 D24, 4781, doi:10.1029/2002JD002259.

661

662 Tselioudis G, Rossow W, Zhang Y, Konsta D, 2013: Global weather states and their properties  
663 from passive and active satellite cloud retrievals. *J Clim* 26:7734–7746. doi:10.1175/JCLI-D-13-  
664 00024.1

665

666 Weare, B., 2004: A comparison of AMIP II model cloud layer properties with ISCCP D2  
667 estimates, *Clim. Dyn.*, 22, 281– 292.

668

669 Webb, M., C. Senior, S. Bony, and J.-J. Morcrette, 2001: Combining ERBE and ISCCP data to  
670 assess clouds in the Hadley Centre, ECMWF and LMD atmospheric climate models, *Clim. Dyn.*,  
671 17(12), 905– 922.

672

673 Williams KD, and G. Tselioudis, 2007: GCM intercomparison of global cloud regimes: present-  
674 day evaluation and climate change response. *Clim Dyn* 29:231–250. doi:10.1007/s00382-007-  
675 0232-2

676

677 Williams, K.D., Webb, M.J., 2009: A quantitative performance assessment of cloud regimes in  
678 climate models. *Clim Dyn* 33, 141–157. <https://doi.org/10.1007/s00382-008-0443-1>

679

680 Winker DM, Vaughan MA, Omar A et al (2009) Overview of the CALIPSO mission and  
681 CALIOP data processing algorithms. *J Atmos Ocean Technol* 26:2310–2323

682

683

684

685

686 **Table 1**

687 CMIP6 models used in the WS analysis with Horizontal resolution and Vertical Layering.

688

Model	Horizontal resolution (lat x lon)	Vertical Layering
CESM2	0.94 x 1.25	32 levels
CNRM-CM6-1	1.40 x 1.41	91 levels
CNRM-ESM2-1	1.40 x 1.41	91 levels
GFDL-CM4	2.0 x 2.5	33 levels
GISS-E2-1-G	2.0 x 2.5	40 levels
GISS-E3-G	1x1.25	102 levels
HadGEM3-GC31-LL	1.25 x 1.875	85 levels
IPSL-CM6A-LR	1.27 x 2.5	79 levels
MRI-ESM2-0	1.12 x 1.125	80 levels
UKESM1-0-LL	1.25 x 1.875	85 levels

689

690

691 **Table 2**

692 ISCCP-H Weather State mean values of cloud parameters.

	DCN	MDS	CIR	PLR	MID	FRW	SHC	STC
Avg PC [hPa]	242.6	433.6	316.3	395.6	606.9	645.1	840.1	725.5
AvgTAU	10.5	10.4	1.2	2.2	9.5	3.2	4	6.3
Total CF [%]	99.5	99.2	79.9	84.5	97.2	40	79.6	90.7

693

694

695 **Table 3**

696 CMIP5 and CMIP6 model WS Normalized RFO Absolute Deviation from the ISCCP-H WS in

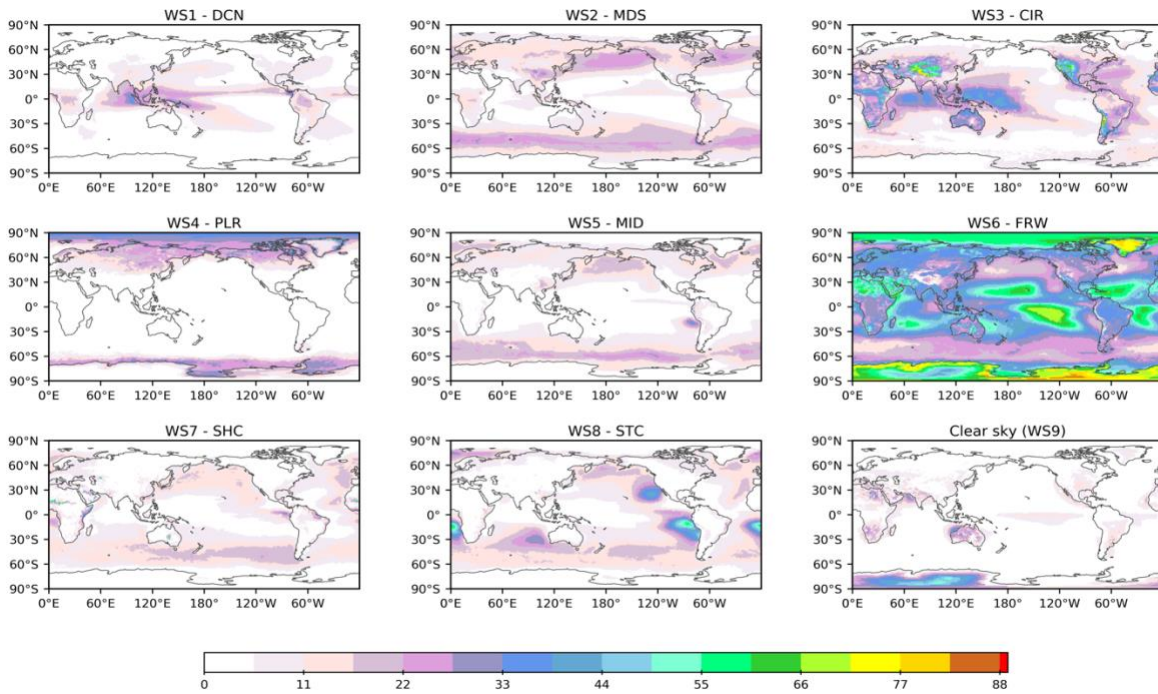
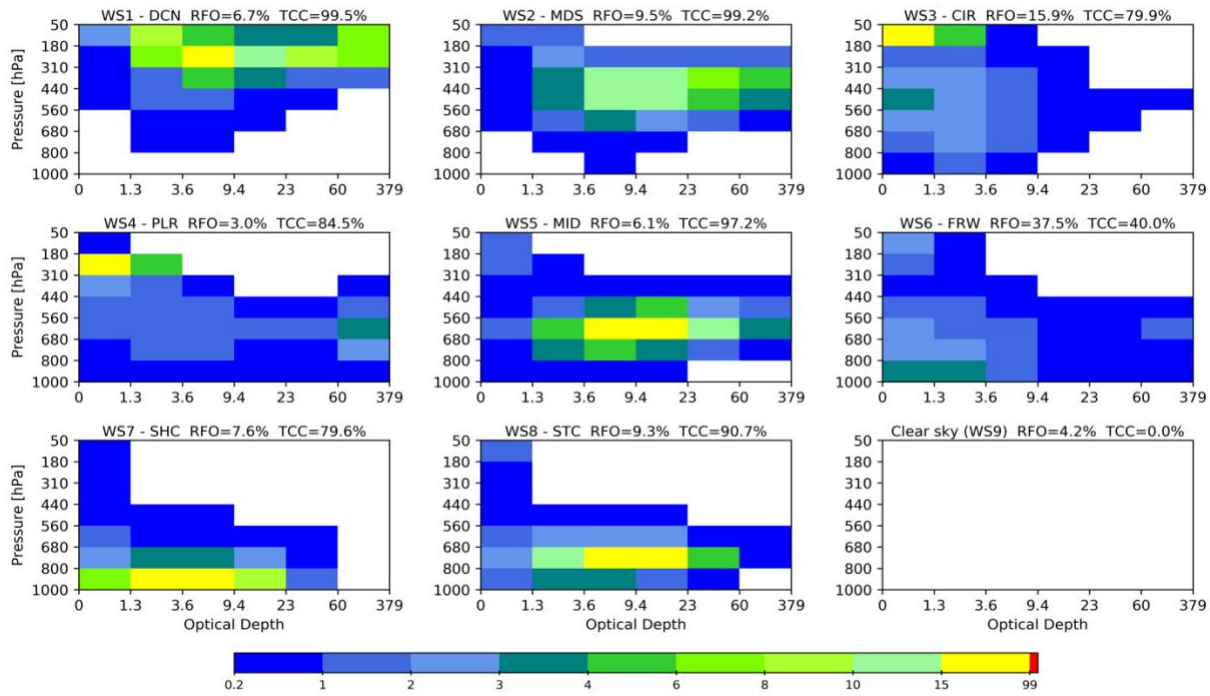
697 %. The quantity is derived by averaging the absolute differences of model WS RFO from the

698 ISCCP-H value and normalizing to the ISCCP-H value.

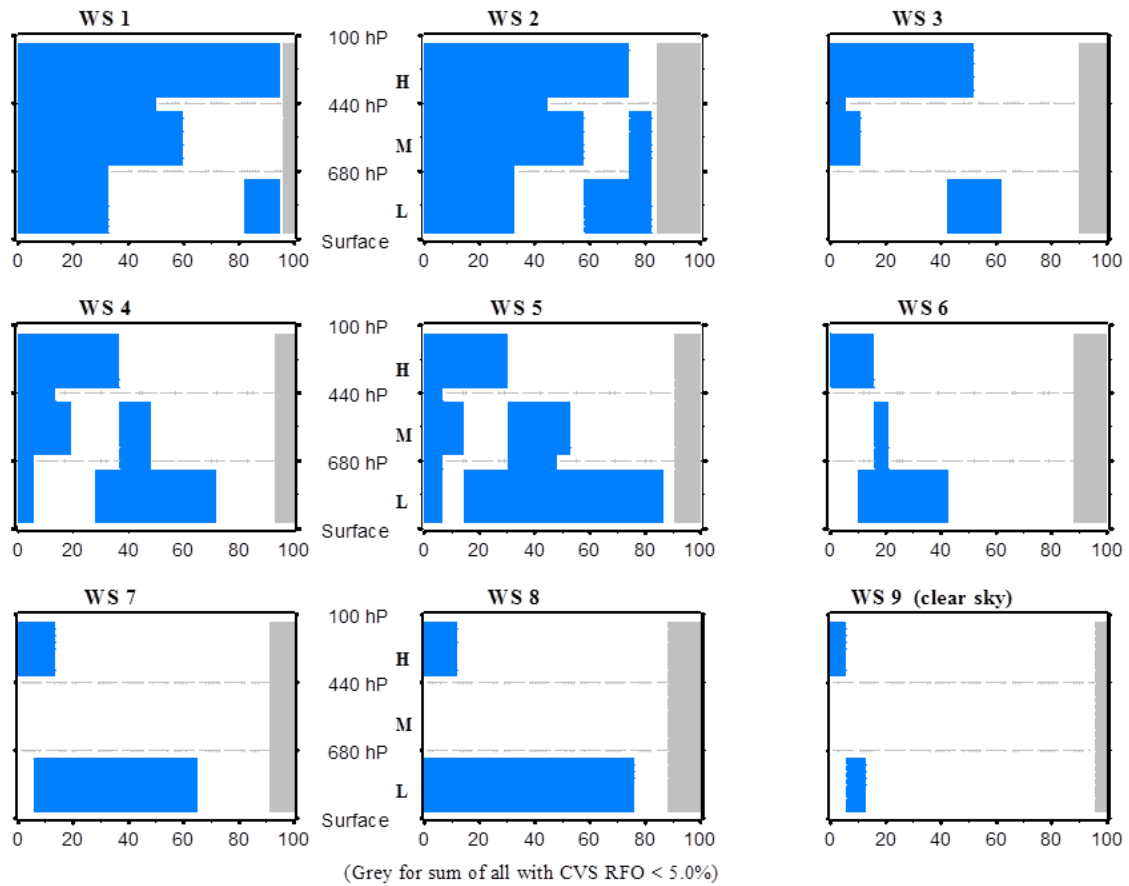
699

	DCN	MDS	CIR	PLR	MID	FRW	SHC	STC	AVG
CMIP6 (%)	21.4	20.9	49.8	69.8	35.8	12.12	48.9	34.9	36.7
CMIP5 (%)	52.2	31.6	24.6	67.7	44.0	19.4	39.7	45.5	40.6

700



702  
 703 Figure 1. (Top) Cloud Top Pressure-Cloud Optical Thickness (PC-TAU) histograms for the eight  
 704 cloud Weather States and a blank histogram (bottom-right) for clear sky. Noted on top of each  
 705 histogram are the Relative Frequency of Occurrence (RFO) and the Total Cloud Cover (TCC).  
 706 (Bottom) Global RFO maps of the 8 cloud WSs and of clear sky.  
 707

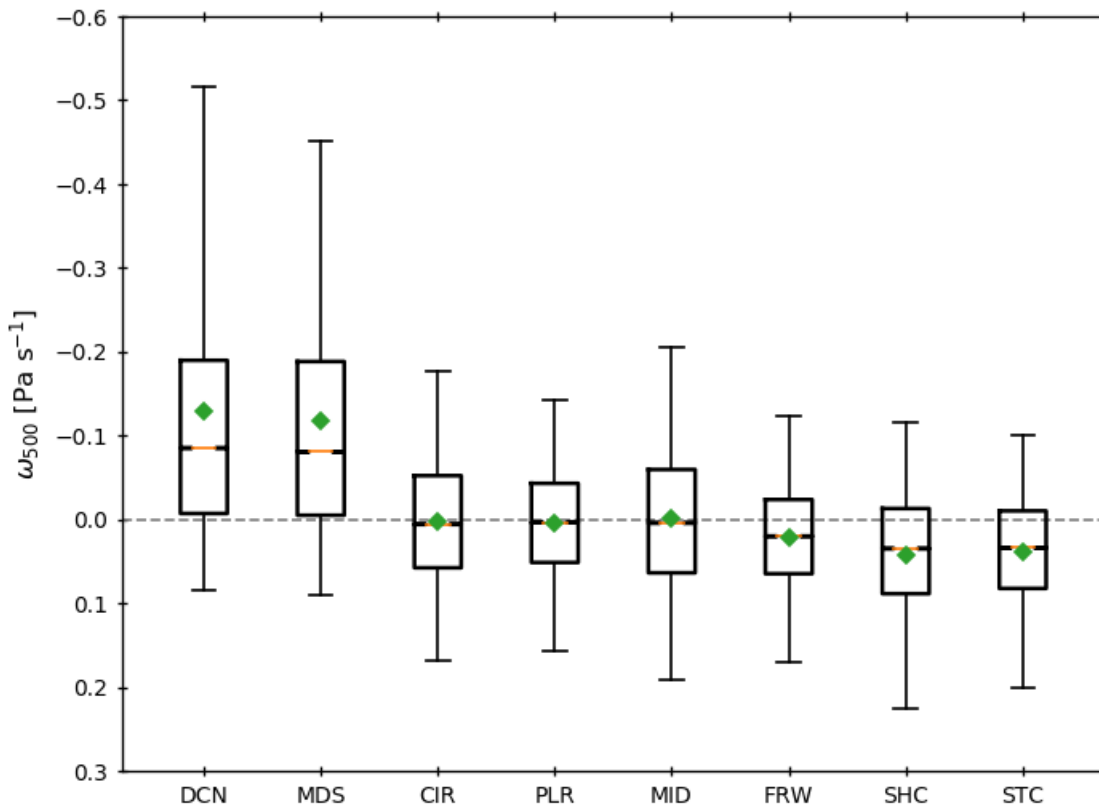


708  
709

710 Figure 2. Cloud Vertical Structure (CVS) distributions for the 8 cloud WSs and for clear sky,  
 711 derived from CloudSat/CALIPSO retrievals. The blue bars indicate cloud presence in a vertical  
 712 layer, and the width of each CVS bar indicates the frequency of occurrence of this CVS in the  
 713 particular WS (see Tselioudis et al. 2013, Fig. 4 for CVS definitions). The white bar (space)  
 714 indicates clear sky, and the gray bar represents the sum of all CVSs that occur less than 5% of  
 715 the time.

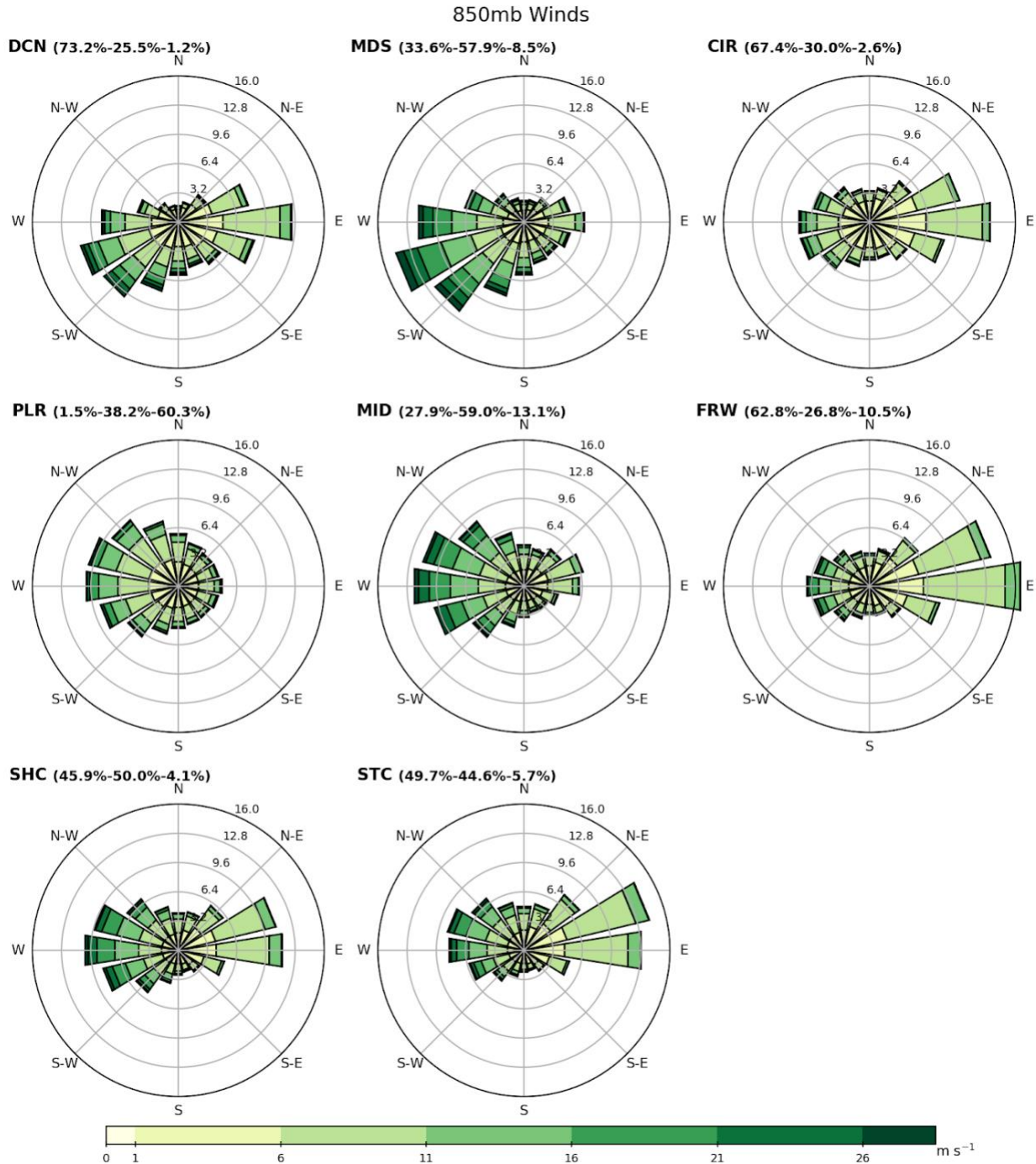
716



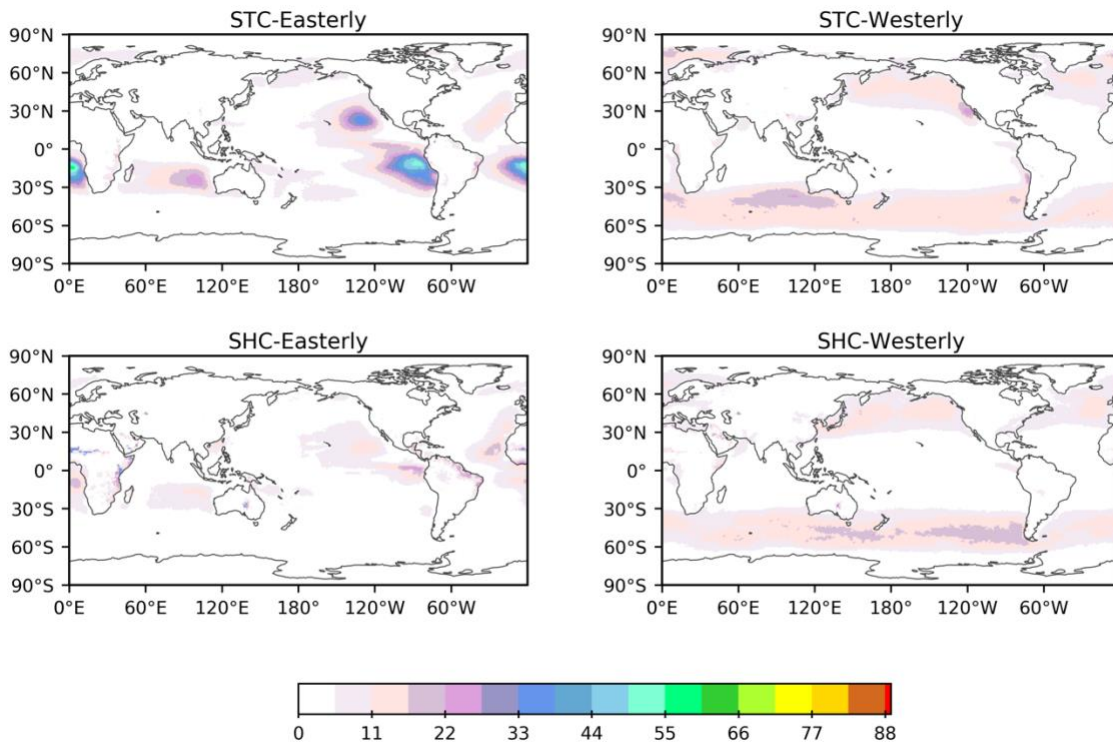


726

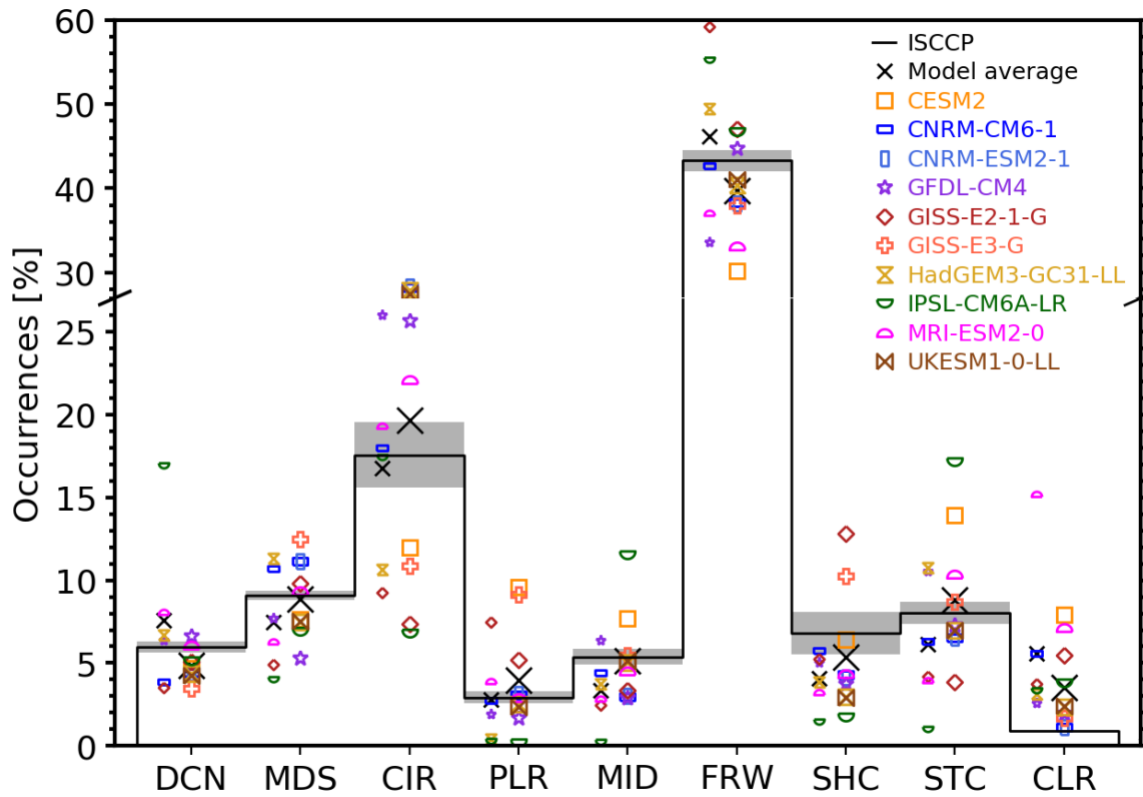
727 Figure 4: Box-and-whisker diagram of ERA-Interim 500-mb vertical velocity distributions for  
 728 the 8 cloud WSs. The line represents the median, the rhombus represents the mean, the box  
 729 represents the 75<sup>th</sup> percentile, and the bar represents the 95<sup>th</sup> percentile of each distribution.



730  
 731 Figure 5: Wind rose diagrams for the 8 cloud WSs, from ERA-Interim 850mb wind data. The  
 732 length of each "spoke" around the circle indicates the fraction of time that the wind blows from a  
 733 particular direction, noted on the circles. Colors along the spokes indicate categories of wind  
 734 speed, noted on the color bar at the bottom of the plot. At the top of each plot, the label shows  
 735 the percentage of time that each WS occurs in the tropical (30S-30N), midlatitude (30-60N/S),  
 736 and polar (60-90N/S) regions.  
 737



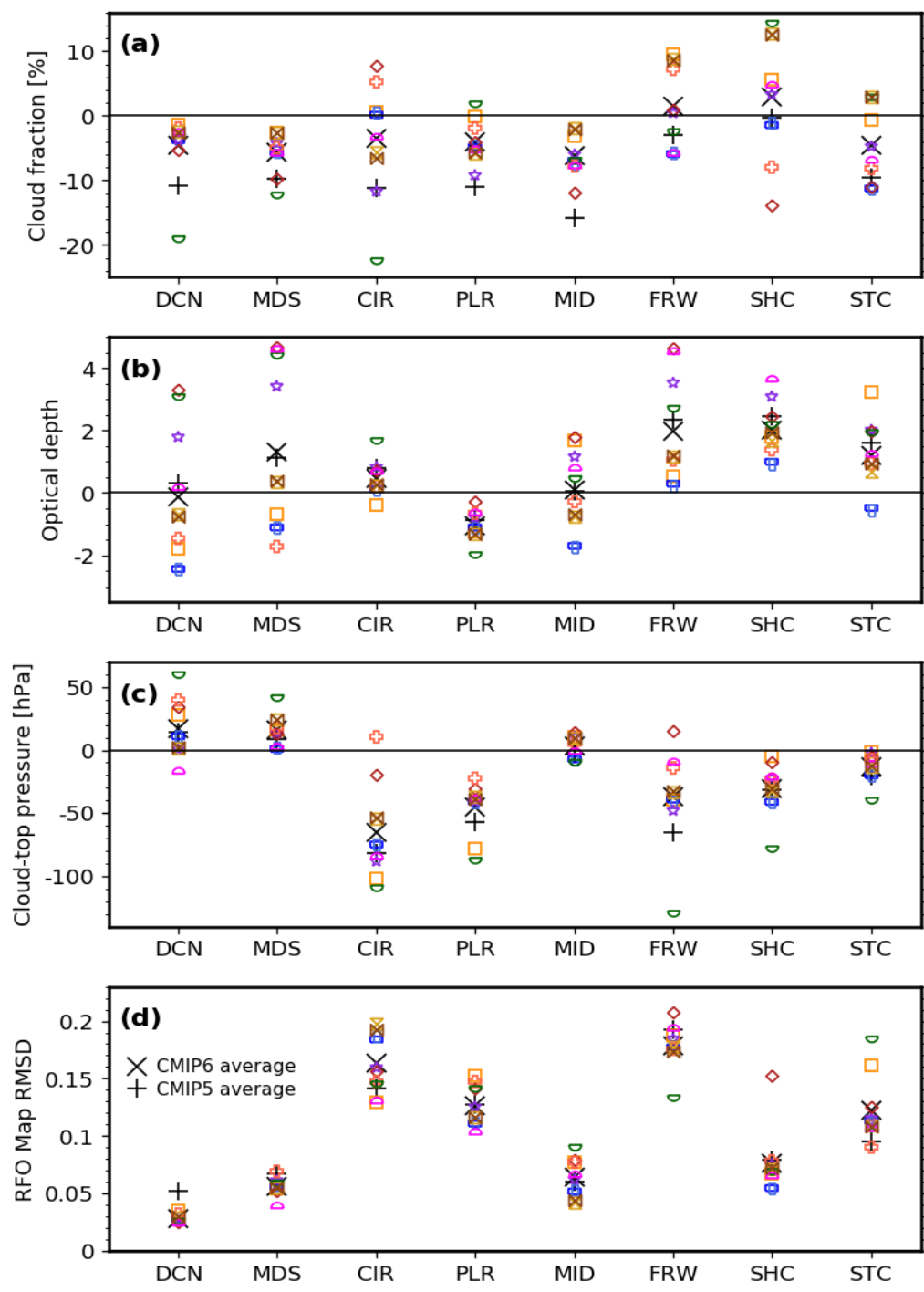
738  
 739 Figure 6. Global maps of the Relative Frequency of Occurrence (RFO) of the Stratocumulus  
 740 (top) and the Shallow Cumulus (bottom) WSs, separately for their easterly wind (left panels) and  
 741 their westerly wind (right panels) components.



742  
743

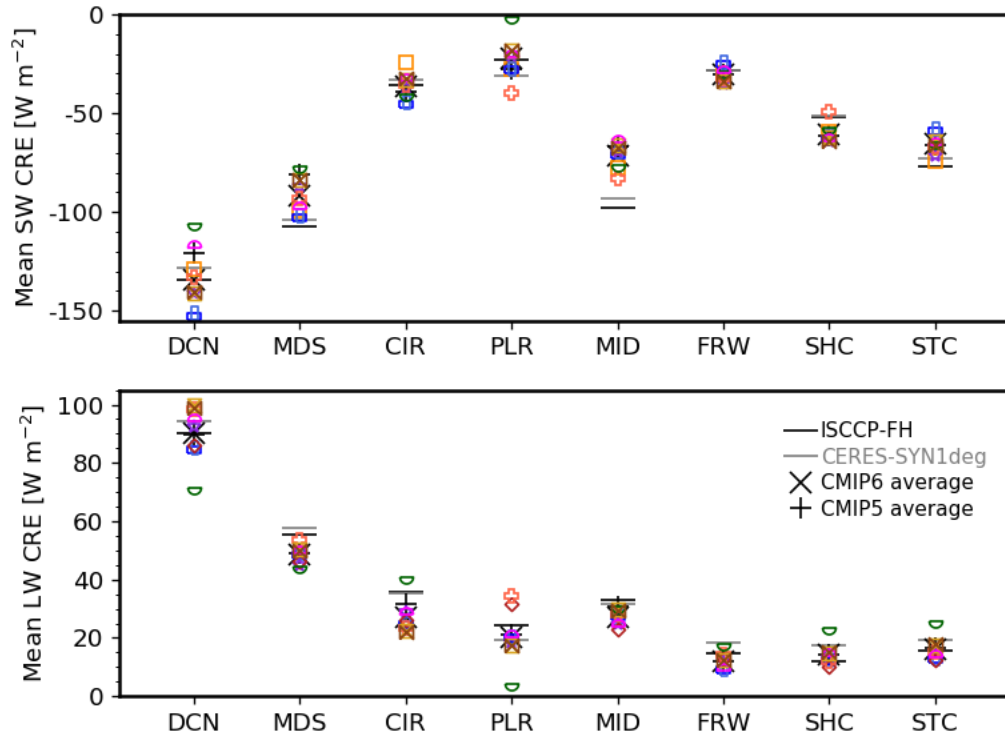
744 Figure 7: Relative frequency of occurrence of the eight cloud WSs and clear sky, from the  
 745 ISCCP-H dataset (solid line) and the AMIP 20<sup>th</sup> century simulations of the CMIP6 and CMIP5  
 746 models (model symbols are indicated in the label). The gray bar around the line indicates the  
 747 ISCCP-H interannual variability. The larger symbols on the right column correspond to the  
 748 CMIP6 versions of the models and the smaller symbols on the left side to the CMIP5 versions of  
 749 the models. The X sign is the mean of each model ensemble.

750



751  
 752 Figure 8: Difference between CMIP6 model and ISCCP-H WS mean (a) cloud fraction, (b) cloud  
 753 optical depth, and (c) cloud top pressure, and (d) Root Mean Square Difference between the WS  
 754 RFO maps of the CMIP6 models and ISCCP-H. The CMIP6 model ensemble mean difference is  
 755 indicated with an X and the CMIP5 one with a +. CMIP6 model symbols are as indicated in Fig.  
 756 6.

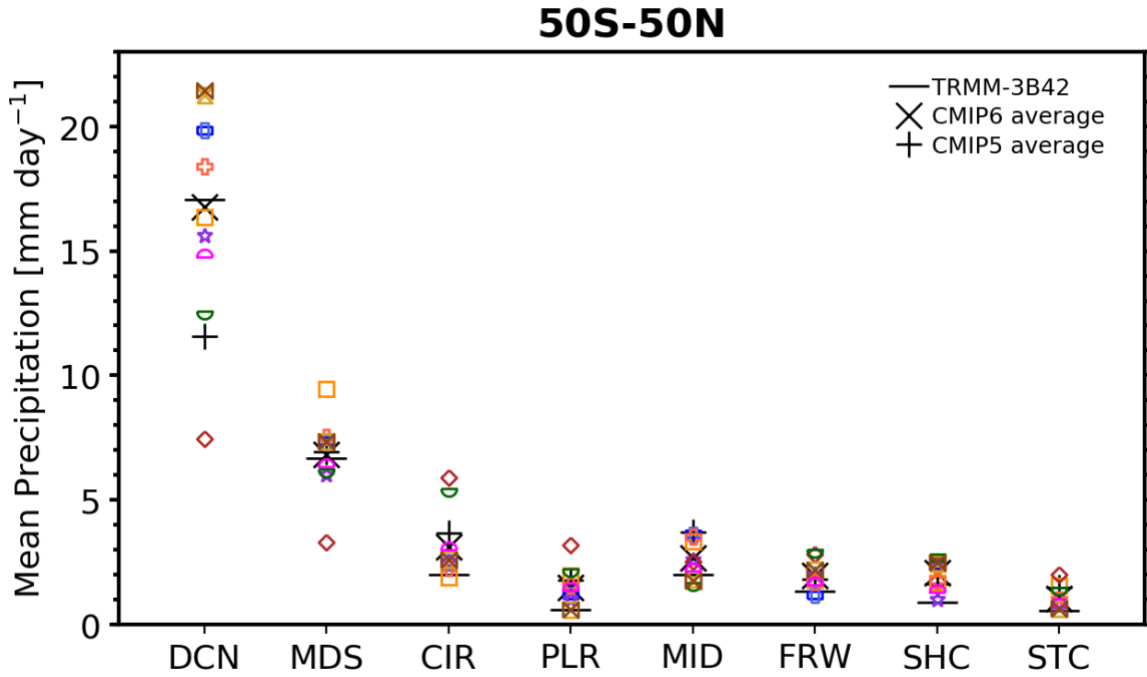
757



758

759 Figure 9: Mean values of CMIP6 model WS (top) Shortwave Cloud Radiative Effect (SW CRE),  
760 and (bottom) Longwave Cloud Radiative Effect (LW CRE). The CMIP6 model ensemble mean  
761 is indicated with an X, the CMIP5 mean with a +, and the mean values for the ISCCP-H WSs  
762 derived from the CERES and the ISCCP-FH radiative flux datasets are noted with horizontal  
763 bars. Model symbols are as indicated in Fig. 6. Positive/negative values indicate radiative  
764 warming/cooling.

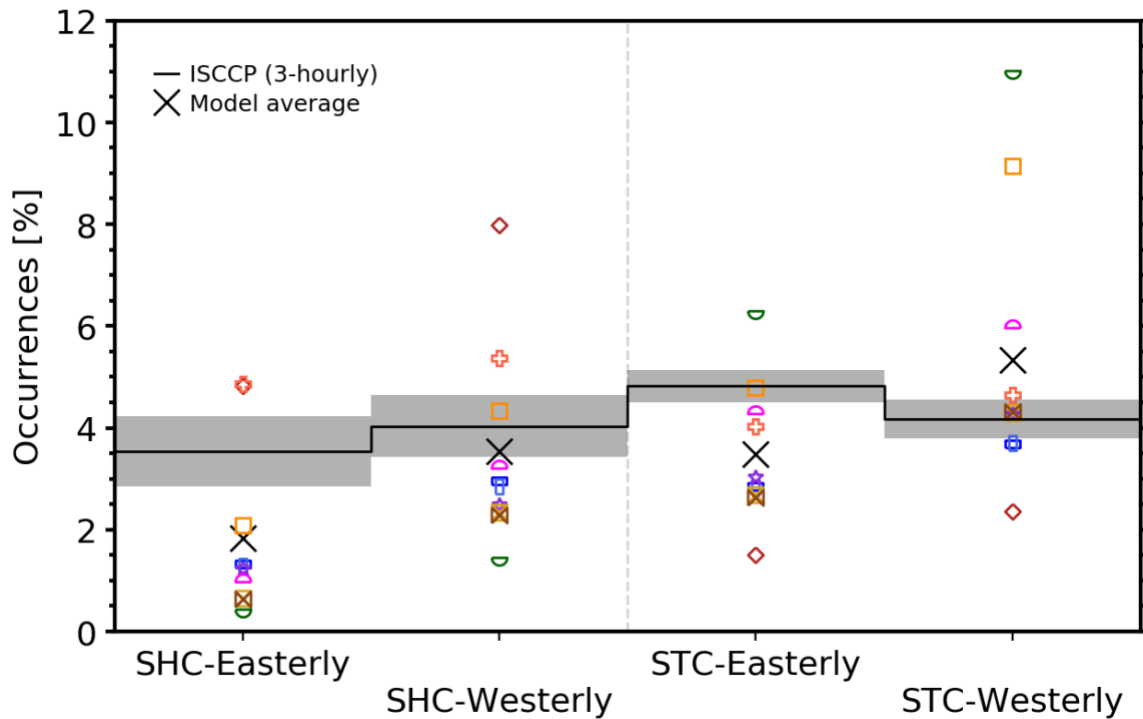
765



766  
767

768 Figure 10: Mean values of CMIP6 model WS precipitation. The CMIP6 model ensemble mean is  
 769 indicated with an X, the CMIP5 mean with a +, and the mean values for the ISCCP-H WSs  
 770 derived from the TRMM precipitation dataset is noted with a horizontal bar. CMIP6 model  
 771 symbols are as indicated in Fig. 6.

772



773

774 Figure 11. Relative frequency of occurrence of the easterly and westerly components of the  
 775 shallow cumulus (SHC) and stratocumulus (STC) WSs, from the ISCCP-H dataset (solid line)  
 776 and the AMIP 20<sup>th</sup> century simulations of the CMIP6 models (model symbols are indicated in the  
 777 label). The gray bar around the line indicates the ISCCP-H interannual variability. The X sign is  
 778 the mean of each model ensemble.